

BRNO UNIVERSITY OF TECHNOLOGY

**FAKULTY ELECTRICAL ENGINEERING
AND COMMUNICATION**

DEPARTMENT OF TELECOMMUNICATIONS

Ing. Pavel Dvořák

**BRAIN TUMOR DETECTION AND SEGMENTATION IN
MULTISEQUENCE MRI**

DETEKCE A SEGMENTACE MOZKOVÉHO NÁDORU V MULTISEKVENČNÍM MRI

SHORT VERSION OF PH.D. THESIS

Specialization: Teleinformatics

Supervisor: Prof. Ing. Zdeněk Smékal, CSc.

Opponents:

Date of Defense:

KEYWORDS

Brain tumor, image analysis, image segmentation, medical imaging, MRI, multisequence imaging, local structure, structure prediction

KLÍČOVÁ SLOVA

Mozkový nádor, analýza obrazů, segmentace obrazů, lékařské zobrazování, MRI, multisekvenční zobrazování, lokální struktura, predikce struktury

Doctoral thesis is available at the Science Department of Dean's Office FEEC, Brno University of Technology, Technická 10, Brno, 616 00

© Dvořák Pavel, 2015

ISBN 80-214-

ISSN 1213-4198

OBSAH

1	Introduction	5
2	Related Work	6
2.1	Brain Tumor Segmentation	6
2.2	Local Structure Prediction	7
3	Goals of the thesis	8
4	Methodology	9
4.1	Brain tumor presence detection	9
4.2	Unsupervised brain tumor extraction	11
4.3	Brain tumor segmentation using local structure prediction	13
5	Results and Discussion	18
5.1	Brain tumor presence detection	18
5.2	Unsupervised 2D brain tumor extraction	21
5.3	Unsupervised 3D brain tumor extraction	24
5.4	Brain tumor segmentation using local structure prediction	27
6	Conclusion	34
	Bibliography	35
	Bibliography of the author	38

1 INTRODUCTION

Based on statistics of the Central Brain Tumor Registry of the United States (CBTRUS), brain tumor is one of the leading cause of cancer-related deaths in the United States. It is the second leading cause of cancer-related deaths in children under the age 20 as well as in males ages 20-39. The most common primary brain tumor, brain tumors that begin and tend to stay in the brain, is meningioma with 34%, however glioma, a broad term including tumors arising from the gluey or supportive tissue of the brain (30% of all brain tumors), represents 80% of malignant tumors making it the most common primary brain tumor causing death. This work is particularly focused on the automatic processing of the volumes with glioma in low and high grades. Due to the increasing number of patients, the number of acquired data increase, too. Therefore, there is increasing necessity of automatic algorithms that are able to process the data automatically. Hence, there have also been increasing interest in developing such algorithms and, particularly, the automatic brain tumor segmentation task has recently attracted many computer vision research teams.

In common clinical routines, the evaluation the acquired images is currently performed manually based on quantitative criteria or measures such as the largest visible diameter in axial slice [9]. Therefore, highly accurate methods being able to automatically analyze scans of brain tumor would have an enormous potential for diagnosis and therapy planning. However, it was shown by Menze et al. [21] that even manual annotation performed by expert raters showed significant variations in areas where intensity gradients between tumorous structure and surrounding tissue are smooth or obscured by bias field artifacts or partial volume effect. Moreover, brain tumor lesions are only defined by relative intensity changes to healthy tissues, and their shape, size and location are individual for each patient, which makes the use of common pattern recognition algorithms impossible.

In this work, three different MR sequences, namely T1-weighted image, T2-weighted image, and FLAIR image. In the brain tumor investigation, T1-weighted images (shortly T1 image) are usually used in combination with contrast agent fluid, which highlights the blood flow here. This cause the tumor active part to appear hyper-intense and easily distinguishable from surrounding tissue. Such image is called “contrast enhanced T1-weighted image” and in this work the abbreviation T1C will be used. T2-weighted images (shortly T2 images) are, compared to T1 images, more sensitive to the content of water and, therefore, to the pathology, which, as well as cerebrospinal fluid (CSF), appear hyper-intense here. Fluid-attenuated inversion recovery (FLAIR) is a sequence that suppresses CSF in brain imaging. This effect enables to distinguish lesions, which remains hyper-intense as in T2 images, from CSF which becomes hypo-intense here.

2 RELATED WORK

2.1 Brain Tumor Segmentation

The automated brain tumor segmentation is still a challenging task. One of the reason is tumor's unpredictable properties such as size, shape and location unless the tumor development in time is investigated and images from previous scanning are available. Considering only the independent scanning, all of the mentioned properties are unknown. Thus common pattern recognition techniques relying on such properties and widely used for object detection and extraction in both medical and real world images cannot be employed. However, other knowledge such as structure of the healthy human brain or tumor manifestation in particular MR sequences can be used. This is, on the other hand, the advantage compared to image object detection, e.g. human or car, where the color and the background scene vary. There have been an increasing interest in developing such algorithms and, particularly, the automatic brain tumor segmentation task has recently attracted many computer vision research teams.

Due to variety of brain tumor types and their manifestation in MR images, most state-of-the-art methods focus on most common tumor types, i.e. glioblastoma, or they require specific training database to deal with a specific tumor type. Only few researchers, e.g. Islam et al. [15], tried to train a developed algorithm on one tumor type and test it on another. However, the results were not satisfying.

Since different brain tumor segmentation methods rely on different image information, the following division will be used in this chapter: threshold-based methods, which rely on the intensity difference between a brain tumor and surrounding tissues, region-based methods, which search for connected regions of voxels with similar properties, contour-based methods searching for edges between a brain tumor and surrounding tissues, classification or clustering methods, which make use of voxel-wise intensity and texture features, and atlas-based methods using the prior knowledge about the healthy brain. However, the division is not always clear because proposed methods often have the same nature and combine more of these approaches. In recent years, most state-of-the-art techniques have been based on atlas guidance [17, 22] and classification. A variety of classification algorithms have been used for this purpose: Support Vector Machine (SVM) [30, 35], Neural Networks (NNs) [3, 23], or Random forest (RF) [11, 20, 26]. A lot of NN-based methods started to appear with the increase of the deep learning popularity [7, 34, 39]. common characteristic of most classification-based algorithms is the independent classification of a single pixel/voxel.

Tumor detection

Apart from tumor segmentation methods, only several methods for detection of the tumor presence and its approximate location exist. The goal of these methods is not the accurate delineation of the tumor boundary, but only fast decision whether the tumor is present together with its location. Such techniques could be used as an initial estimation of the tumor contour

which is necessary for some segmentation methods. Saha et al. [32] located tumors in 2D MR images in axial plane using the fast detection of asymmetry by Bhattacharyya coefficient. The output of the algorithm was the bounding box around the tumor. Farjam et al. [10] used template-matching technique for this purpose.

2.2 Local Structure Prediction

Medical images show high correlation between the intensities of nearby voxels and the intensity patterns of different image modalities acquired from the same volume. Patch-based prediction approaches make use of this local correlation and rely on dictionaries with finite sets of image patches. They succeed in a wide range of application such as image denoising, reconstruction, and even the synthesis of image modalities for given applications [14]. Moreover, they were used successfully for image segmentation, predicting the most likely label of voxels in the center of a patch [33]. All of these approaches exploit the redundancy of local image information and similarity of *image features* in nearby pixels or voxels. For most applications the same local similarity is present among the *image labels*, e.g., indicating the extension of underlying anatomical structure. This structure has already been used in medical imaging but only at *global level*, where the shape of the whole structure is considered, e.g. [27, 36].

The first attempt to predict extended 2D patches instead of pixel-wise labels was made by Zhu et al. in [37] and later in [38], who proposed a recursive segmentation approach with recognition templates in multiple layers called Hierarchical Image Models (HIM) for image parsing using structured perceptron learning. A label patch dictionary is defined manually. Such approach is suitable for approximate delineation of an object in natural image processing but not for accurate segmentation of medical images.

Kontschieder et al. [16] extended the previous work with structured image labeling using random forest. They introduced a novel data splitting function based on random pixel position in a patch, and exploited joint distributions of structured labels. They used image patches of fixed size of 24×24 pixels and label patches of size 11×11 .

Chen et al. [4] used CRF for shape epitome prediction of a given image patch and called their model Shape epitome CRF (SeCRF). The shape epitomes are created using affinity propagation [12] of patches extracted around the image ground truth boundaries. These patch epitomes are represented by a group of shape templates of smaller size, which are generated by translation and rotation of a template mask within the patch epitome.

Dollar et al. [8] used the idea from [16] to create an edge detector based on the patch structure prediction using k -means clustering in the label space to generate an edge dictionary, and RF to predict the most likely local edge shape. They used label patches of size 16×16 to be assign to larger 32×32 image patches with stride of 2. They run the prediction for three different scales, the original image and a half and double resolution version.

3 GOALS OF THE THESIS

This chapter describes the objectives and goals of the thesis. The main goal is to develop algorithms for brain tumor detection and segmentation in 2D and 3D single- or multisequence MRI. The proposed methods have to be fully automated, i.e. they have to be able to detect and segment brain tumor without a user interaction. Even though the user interaction is sometimes necessary and even appreciated, e.g. for post-processing correction, the proposed methods must not be based on any kind of user interaction. The proposed methods should be primarily focused on dealing with glioma of both low and high grades. The attention during the algorithms development should be paid to the segmentation accuracy as well as to the computational demands during the segmentation process.

4 METHODOLOGY

The goal of this chapter is to contribute to the medical image analysis domain, specifically to the field of brain tumor detection and segmentation in multisequence MR images. Three proposed methods are described: a fast pathology presence detection approach, which is based on multi-resolution symmetry analysis, an unsupervised extraction algorithm of glioma, and a supervised approach of three brain tumor segmentation sub-problems (segmentation of whole tumor, tumor core, and active tumor).

Most of the segmentation algorithms require pre-processing applied to the input image. In brain MRI processing, this usually includes spatial co-registration, bias field correction, intensity normalization, and skull stripping. All data sets used during the evaluation of the proposed methods had been pre-processed before they were released. Therefore, this work does not deal with pre-processing algorithms.

4.1 Brain tumor presence detection

The method proposed for brain tumor presence detection is a symmetry based algorithm for the detection of a brain tumor presence in 2D MR slice. It is a modification and extension of a method that I have already published in [54, 56]. The algorithm uses the fact that brain tumors break the approximate tissue structure symmetry in the left and right hemisphere, which is usual for healthy brains.

The symmetry prior requires another pre-processing step: mid-sagittal plane detection. This has been studied in several works, e.g. [19, 31]. Another approach uses registration of the brain volume to a reference aligned volume, which may be based on the same methodology described in the section about pre-processing. The proposed method is not sensitive to small deviations from perfect alignment and is able to work correctly even with slight rotation.

The proposed method was designed for both axial and coronal planes. It is a supervised classification algorithm, which uses features extracted from multiresolution asymmetry maps and, in case of application to particular slices in 3D volume, input slices. The latter type of features, based on the input image, are not applicable for stand-alone slices since the intensities in such slices varies due to different measurement parameters and equipment, and the intensity normalization is not possible. Random forest (RF) [6] is used as a classification algorithm but another supervised algorithm may be used.

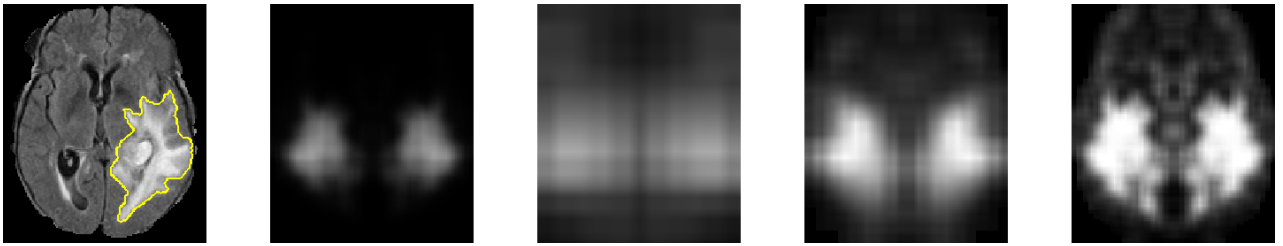
Symmetry analysis

A square block, with the side length of 10 voxels is created. This size used in multiresolution approach is suitable for the detection of both small and large tumors. The algorithm slides through both halves symmetrically by this block. The step size is smaller than the block size to ensure the overlap of particular areas that are compared with its opposite symmetric part.

Normalized histograms with the same range are computed from both parts and compared by the Bhattacharyya coefficient (BC) [2]. The range of values of BC is $\langle 0, 1 \rangle$, where the smaller the value, the bigger the difference between histograms. For the subsequent purposes, an Asymmetry coefficient (AC) is computed as $AC = 1 - BC$. The computed ACs create an asymmetry map where the higher value expresses the higher probability of the tumor presence in particular location.

Multiresolution approach. To make the whole process of the symmetry analysis robust, the image is processed in the same way in several different resolutions with constant block size. The input image is iteratively sub-sampled by the factor of two. The number of iterations performed during the symmetry analysis was experimentally set to three.

The output of each iteration is a map of anomalies for a given resolution. This anomaly map is both sided and, hence, the healthy regions, where the tumor is present at the opposite side, are also labeled with high probability of a brain anomaly. The product of values corresponding to a particular pixel is computed leading to the final multiresolution asymmetry map. An example of such multiresolution asymmetry map is depicted in Fig. 4.1.



Obr. 4.1: Example of a brain tumor multiresolution asymmetry map. The input image is depicted on the left followed by the multiresolution asymmetry map and corresponding single-resolution asymmetry maps with increasing image resolution.

Feature extraction

When the asymmetry maps are generated, they are used for extraction of features, which are then used for binary image classification into two groups of images showing a healthy or pathological brain. The extracted features are as follows:

- maximum of the multiresolution asymmetry map,
- maximum of each singleresolution asymmetry map,
- number of regions and their size after thresholding the multiresolution map by an absolute value,
- number of regions and their size after thresholding the multiresolution map by a relative value.

Five different levels of threshold are set for both relative and absolute thresholding leading to five values of each feature.

Application to 3D volumes

The proposed algorithm may also be applied to particular slices in 3D volumes. In this case, additional set of features can be extracted. This feature set assumes that the intensities of the input volume has been normalized. The intensity features are based on the same multi-resolution asymmetry map thresholding, but the information is extracted from the input slice. For each threshold level, four more features are extracted from the input image after the application of the mask created by thresholding. The features are as follows:

- average intensity in the whole masked region,
- absolute value of the average intensity difference in the left and right masked region,
- intensity standard deviation in the whole masked region,
- absolute value of the intensity standard deviation difference in the left and right masked region.

All of these features are computed for both absolute and relative value thresholding.

4.2 Unsupervised brain tumor extraction

Gliomas are represented by high intensities in T2 and FLAIR sequences. However, considering different measurement parameters and equipments, the intensities in the resulting image are not known. The common approach is to normalize the intensities by standardization or histogram matching algorithm. Considering a stand-alone 2D MR slice, such intensity normalization is impossible due to the lack of information about the tumor size and the slice position. Therefore, machine learning approaches based on the intensity information are not applicable here. The proposed algorithm avoids the intensity normalization by automatic determination of the intensity threshold from the most asymmetric brain parts. It is based on the same symmetry analysis described in Sec. 4.1. Hence, the method requires the same pre-processing as the method proposed for the supervised brain tumor detection. The method can be applied for both 2D image and 3D volume. Only FLAIR images are used for 2D image application while both sequences are used for 3D volume application. I have already described this method in [48, 50].

Pathology extraction

For the pathology extraction purpose, thresholding of the multi-resolution asymmetry map is performed by the value of 10% of the maximum asymmetry. This value was set experimentally and ensures that at least small region is extracted. The result is a both-sided mask that contains both the tumor on one side and the healthy tissue on the other side.

Since multifocal tumor can appear, the extraction process is not limited to only one region. All regions created by thresholding are considered. As a result, multifocal tumors located asymmetrically can be correctly detected.

The whole area of glioma can be well separated using FLAIR, since they appear hyperintense in this MR sequence. The automatic thresholding can be performed to extract these pathological areas. The threshold is determined using the Otsu's method [24] from the points inside the resulting mask of asymmetry detection but the thresholding process is applied to the whole image.

Morphological erosion and dilation are applied to the resulting mask to smooth the region borders and separate regions connected by a thin area. The conjunction of these masks is then found. Since some incorrect areas could be extracted, only those, which are situated mostly inside the asymmetric region, are labeled as pathological. Regions with the size smaller than 10% of the largest segment are also eliminated. Since the pathological area may extend beyond the asymmetry area border, the whole region created by the thresholding is extracted.

Extension into 3D

The same algorithm may be applied to 3D volumes. The multi-resolution asymmetry map is computed in the exactly same way but in 3D instead of 2D, i.e. cubic blocks are used instead of square blocks. I have already described this 3D extension in [44, 51].

The extraction process starts in the axial slice where the highest AC was detected and it is then propagated into the whole 3D volume. Such approach is more accurate than the extraction directly from the 3D asymmetry map. However, it is slightly slower. For the 3D extraction purpose, T2 volume is used together with FLAIR to improve the accuracy. Since brain tumor appears hyper-intense in both T2 and FLAIR images, the same algorithm is applied to both volumes and their intersection is found.

The resulting mask \mathbf{M} of the extraction process is created as $\mathbf{M} = \mathbf{M}_{T2} \cap \mathbf{M}_{FLAIR}$, where \mathbf{M}_{T2} and \mathbf{M}_{FLAIR} are the thresholding mask of T2-weighted and FLAIR images, respectively.

Propagation into neighbor slices. Once the pathology is extracted from the axial slice with the highest asymmetry coefficient, it can be propagated into other slices. At first both 3D volumes are thresholded using the particular threshold values determined in the initial slice with the highest asymmetry. In order to avoid extraction of healthy areas far from the pathological ones, the propagation of mask estimated in neighbor slice is necessary.

The propagation process starts with both neighbor axial slices and continues in both directions. The result for n -th slice can be defined as:

$$\mathbf{M}(n) = \mathbf{M}_{T2}(n) \cap \mathbf{M}_{FLAIR}(n) \cap \mathbf{M}_D(n \pm 1), \quad (4.1)$$

where $\mathbf{M}_D(n \pm 1)$ is the dilated mask from neighbor slice where the sign depends on the propagation direction.

4.3 Brain tumor segmentation using local structure prediction

In spite of the success of patch-based labeling in medical image annotation, and the highly repetitive local label structure in many applications, the concept of local structure prediction as described in Chapter 2.2 has not received attention in the processing of 3D medical image yet. However, approaches labeling supervoxels rather than voxels has already appeared, e.g. hierarchical segmentation by weighted aggregation extended into 3D by Akselrod-Ballin et al. [1] and later by Corso et al. [5], or spatially adaptive random forests introduced by Geremia et al. [13]. Several structure-based methods has also been used in medical imaging but only at *global level*, where the shape of the whole segmented structure is considered, e.g. [27, 36]. Here, the presented work will focus on *local structure* since global structure is not applicable for objects with various shapes and locations such as brain tumors.

The proposed method transfers the idea of *local structure prediction* [8] using patch-based label dictionaries to the task of dense labels of pathological structures in multisequence 3D volumes. Different from Dollar, convolutional neural networks are used for predicting label patches as they are well suited for dealing with local correlation, also in 3D medical image annotation tasks [18] [28].

The brain tumor segmentation problem consists of three sub-problems: identifying the whole tumor region in a set of multisequence images, the tumor core region, and the active tumor region [21]. All three sub-tasks are processed separately, which changes the multi-class segmentation task into three binary segmentation sub-tasks.

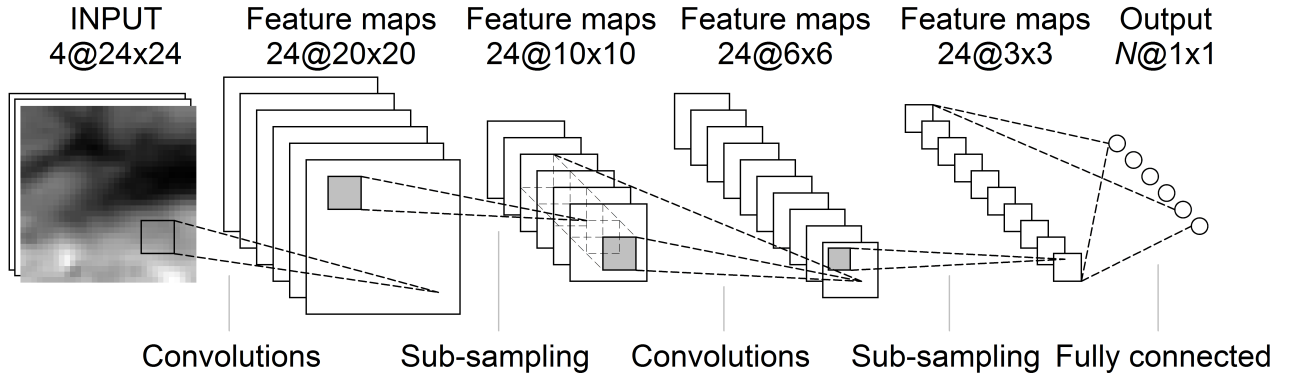
The novelty of this work lies in the principled combination of the deep learning approach together with local structure prediction in the medical image segmentation task. A paper describing the proposed method has been accepted for publication [57].

Convolutional neural network (CNN) is used as a classification algorithm as it has the advantage of preserving the spatial structure of the input, e.g., 2D grid for images. It is a type of modern Deep learning methods.

Convolutional Neural Network (CNN)

This architecture is designed to take the advantages of a 2D grid input, which is convenient for image processing. In several recent works [28, 34], 3D filters have been proposed for medical image analysis. However, it was shown by Prasoon et al. [28] that it is still too demanding to be efficiently used in today's computers.

The CNN architecture used in this work is depicted in Fig. 4.2. It consists of two convolutional and two mean-pooling layers in alternating order. In both convolutional layers, 24 convolutional filters of kernel size 5×5 are used. The input of the network is an image patch of size $4 \times d \times d$ (four MR sequences are present in multisequence volumes) and the output is a vector of length N indicating membership to one of the N classes in the label patch dictionary.



Obr. 4.2: Architecture of the CNN for $d = 24$. The input of the network is a multisequence image patch. The output of the network are N probabilities, where N denotes the size of a label patch dictionary.

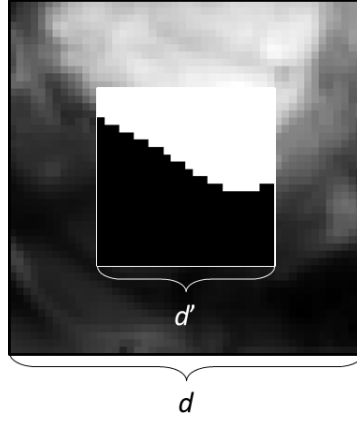
Local structure prediction

This section describes a novel approach for classification-based medical image segmentation techniques, which lies in the principled combination of a deep learning approach together with local structure prediction in the medical image segmentation task. This approach takes the advantage of the fact that most medical images feature a high similarity in the intensities of nearby pixels and a strong correlation of intensity profiles across different image modalities. One way of dealing with – and even exploiting – this correlation is the use of local image patches. In the same way, there is a high correlation between nearby labels in image annotation, a feature that is used in the "local structure prediction" of local label patches.

Let \mathbf{x} be the *image patch* of size $d \times d$ from the image space \mathcal{I} . Focusing on 2D patches, a patch \mathbf{x} is represented as $\mathbf{x}(u, v, I)$ where (u, v) denotes the patch top left corner coordinates in a multisequence image $I(s, V)$ where s denotes the slice position in a multisequence volume V .

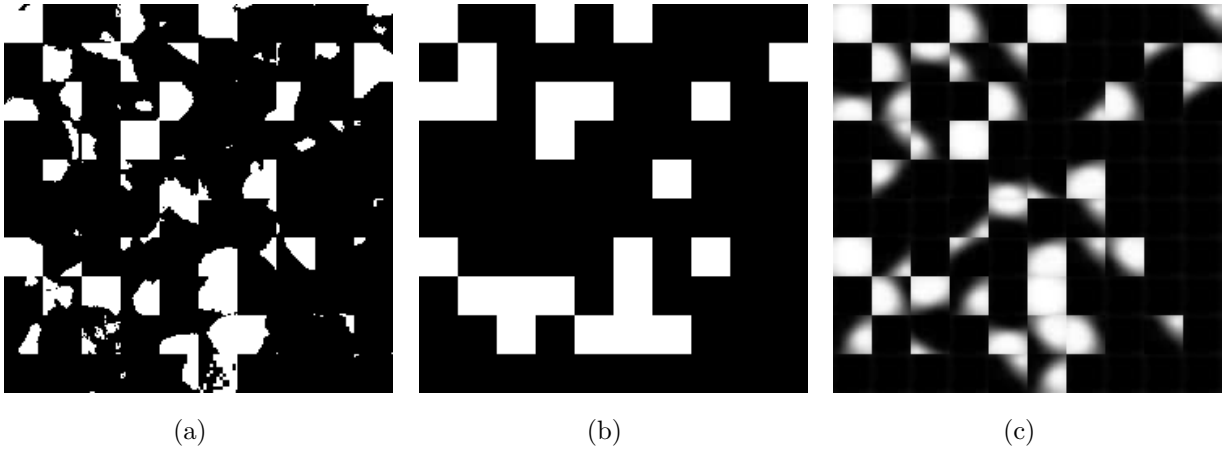
Label patches Treating the annotation task for each class individually, a label space $\mathcal{L} = \{0, 1\}$, which is given by an expert's manual segmentation of the pathological structures, is obtained. The *label patch* is then a patch \mathbf{p} of size $d' \times d'$ from the structured label space \mathcal{P} , i.e. $\mathcal{P} = \mathcal{L}^{d' \times d'}$. The label size d' is equal or smaller than the image patch size d . The label patch \mathbf{p} is centered on its corresponding image patch \mathbf{x} (Fig. 4.3), and it is represented as $\mathbf{p}(u + m, v + m, L)$ where $L(s, W)$ is a manual segmentation in a slice s of a label volume W and m denotes the margin defined as $m = \frac{1}{2}(d - d')$. Optimal values for d and d' and, hence, the ratio $r = \frac{d'}{d}$ may vary depending on the structure to be segmented and the image resolution.

Generating the label patch dictionary Label patches \mathbf{p} are clustered into N groups using k -means leading to a label patch dictionary of size N . Subsequently, the *label template* \mathbf{t} of a group n is identified as the average label patch of a given cluster. In the segmentation process,



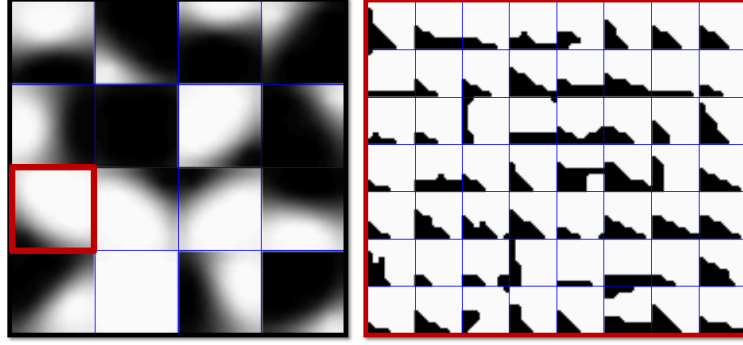
Obr. 4.3: Local structured prediction: Image feature patches (with side length d) are used to predict the most likely label patch (with side length d') in its center. While standard patch based prediction approaches use $d' = 1$ (voxel), the proposed approach considers all values with $1 \leq d' \leq d$.

these smooth label templates \mathbf{t} are then used for the segmentation map computation rather than strict border prediction as used in previous local structure prediction methods [4][16][38]. The structures are learned directly from the training data instead of using predefined groups as in [38]. An example of ground truth label patches with their representation by a dictionary of size $N = 2$ (corresponding to common segmentation approach) and $N = 32$ is depicted in Fig. 4.4.



Obr. 4.4: Ground truth label patches (a) with corresponding binary (b) and structured (c) representation.

The size of the label patch dictionary N and, hence, the number of classes in the classification problem, may differ between problems depending on variability and shape complexity of the data. Figure 4.5 shows an example of clustering training labels patches into 16 classes. The left side of the figure depicts the average labels of each cluster, while the right side shows a subset of train labels assigned to a cluster with a given average patch, i.e. the labels that would be replaced by the same average label in the original image.



Obr. 4.5: Example of clustering the training labels patches into 16 groups. Left: average labels estimated for each group. Right: subset of 56 train labels assigned to a group with the average patch highlighted by a red bounding box in the left image.

Defining the N -class prediction problem After having obtained a set of N clusters, the binary segmentation problem is transformed into an N class prediction task: Each image patch \mathbf{x} is identified in the training set with the group n that the corresponding label patch \mathbf{p} has been assigned to during the label patch dictionary generation. In prediction, the label template \mathbf{t} of the predicted group n (size $d' \times d'$) is assigned to the location of each image patch and all overlapping predictions of the neighborhood are averaged. According to the experiments, a discrete threshold $th = 0.5$ was chosen for final label prediction.

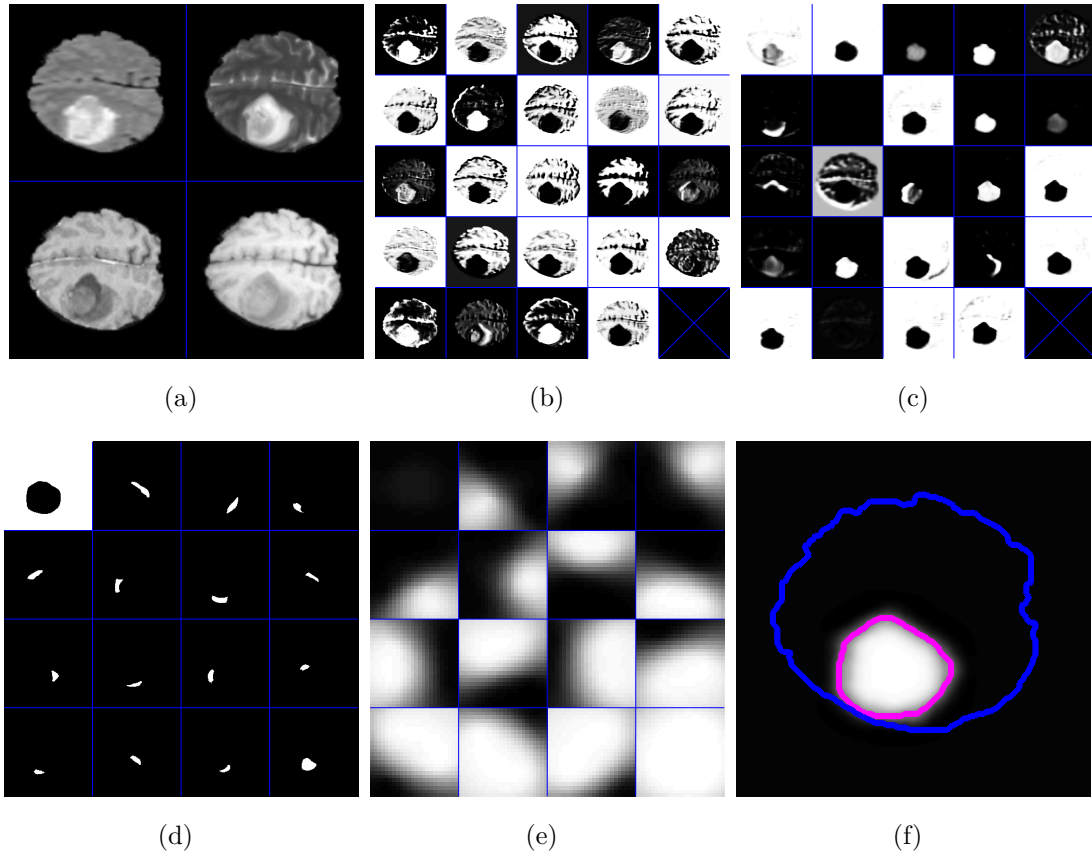
Slice Inference

Image patches from multisequence volumes are mapped into m 2D input channels of the network, where m denotes the number of sequences. This is similar to RGB image mapping. During the training phase, patches of a given size are extracted from training volumes. Using the same approach for testing is inefficient and therefore different approach used in [25] is employed instead. The whole input multisequence 2D slice is fed to the network architecture, which leads to a significantly faster convolutional process than applying the same convolution several times to small patches. This requires proper slice padding to be able to label pixels close to the slice border.

The output of the network is a map of label scores. However, this label map is smaller than the input slice due to the presence of pooling layers inside the CNN architecture. Two 2×2 pooling layers are present in the proposed architecture, which means that there is only one value for every 4×4 region. Pinheiro and Collobert [25] fed the network by several versions of input image shifted on X and Y axis and merged the outputs properly. More common

approach is to upscale the label map to the size of the input image. The latter approach is faster since only one convolution per slice is performed compared to 16 when using the former approach in case of the proposed CNN architecture. Both of them were tested and compared.

One can see the sequential processing of the input multisequence slice in Fig. 4.6. 4.6(b) and 4.6(c) depict 24 outputs of the first and the second convolutional layer of the proposed CNN architecture. 4.6(d) shows the final classification map of the network. Note the average labels for each group in 4.6(e). One can compare them to the ground truth tumor border in the input image. The final probability map of the whole tumor area is depicted in 4.6(f).



Obr. 4.6: Sequential processing of multisequence slice (a). (b) and (c) show all 24 outputs of the first and the second convolutional layer of the proposed CNN architecture. (d) depicts the output of the whole network for 16 groups with the average patch labels depicted in (e). (f) shows the final probability map of the whole tumor area with outlined brain mask (blue) and final segmentation (magenta) obtained by thresholding by $th = 0.5$.

5 RESULTS AND DISCUSSION

This chapter describes all tests that were performed for all three algorithms. The description of the experiments is in the same order as the algorithms description in Chap. 4, i.e. supervised 2D brain tumor presence detection, unsupervised 2D and 3D brain tumor extraction, and supervised brain tumor segmentation in 3D volumes using local structure prediction. The Dice score, Precision, Sensitivity and Accuracy were used for the evaluation purpose. The extraction and segmentation algorithms use the same criteria, while only several of them are used to evaluate the presence detection algorithm. The overall algorithm performance as well as the performance for high-grade (HG) and low-grade (LG) gliomas is evaluated. For each test, the average computing time for the test database is also mentioned. These times do not include the inhomogeneity correction, skull stripping and image co-registration since all data sets had been preprocessed before they were released. All experiments were run on 4-core CPU Intel Xeon E3 3.30GHz without GPU acceleration using Matlab.

All algorithms were tested on publicly available data from the MICCAI 2014 Challenge on Multimodal Brain Tumor Image Segmentation (BRATS ¹). The data set contains 254 real multisequence volumes of 199 high-grade and 55 low-grade glioma subjects. For brain tumor presence detection and brain tumor segmentation using local structure prediction, the data set was divided into three groups: training, validation and testing. The training set consists of 130 high-grade and 33 low-grade glioma subjects, the validation set consists of 18 high-grade and 7 low-grade glioma subjects, and the testing set consists of 51 high-grade and 15 low-grade glioma subjects, summing up to 254 multisequence volumes of average size $240 \times 240 \times 155$. For unsupervised brain tumor extraction, all 254 volumes were used for testing since no training phase is required there.

5.1 Brain tumor presence detection

In this section, the method proposed for detection of particular structures of brain tumor, i.e. whole tumor, tumor core, and active tumor, is evaluated. This method is based on a novel approach using multiresolution symmetry analysis described in Sec. 4.1.

Experimental setup

This algorithm was tested for all four MR sequences, i.e. FLAIR, T2, T1 and T1C. Since brain symmetry exists in two planes, axial and coronal, both of them were considered and tested separately during the algorithm evaluation. Note that slices with tumor core and active tumor are also included in the set of slices with whole tumor; therefore the total number of slices is equal to the sum of whole tumor and healthy slices.

The numbers of pathological slices (with a pathology of size $\geq 100\text{px}$, i.e. a pathology of size $\geq 1\text{cm}^2$ considering the 1mm isotropic resolution) and healthy slices (with no tumor

¹<http://www.braintumorsegmentation.org>

region) in axial and coronal planes are summarized in Tables 5.1 and 5.2, respectively. This table shows the distribution of the data set in training, validation and testing subsets.

Tab. 5.1: Experimental setup of brain tumor presence detection in axial plane.

	Whole tumor	Tumor core	Active tumor	Healthy	Overall
Train	10572	6741	4910	9820	20392
Validation	1553	1057	708	1639	3192
Test	4335	3099	2442	4268	8603
Overall	16460	10897	8060	15727	32187

Tab. 5.2: Experimental setup of brain tumor presence detection in coronal plane.

	Whole tumor	Tumor core	Active tumor	Healthy	Overall
Train	9887	4369	1922	11323	21210
Validation	1449	758	307	1883	3332
Test	4176	2353	1079	4859	9035
Overall	15512	7480	3308	18065	33577

The total number of extracted features from stand-alone images was 24 per sequence, as described in Sec. 4.1. The overall number of features extracted from slices in 3D volume increased to 64 by employing asymmetry-based intensity features.

Application to the test set

Stand-alone slices. The accuracy of whole tumor, tumor core, and active tumor detection in axial and coronal slices is shown in Tables 5.3 and 5.4, respectively. In the tables, one can see that the best accuracy is achieved in FLAIR or T2 images. When all MR sequences are combined, the accuracy is improved for all detected structures.

Presence detection in 3D volumes. This test used the same experimental setup as the evaluation of presence detection in stand-alone images. However, image features are extracted together with the asymmetry features used in stand-alone image, because intensities can be normalized in whole 3D volumes. The accuracy of whole tumor, tumor core, and active tumor detection are shown in Tables 5.5 and 5.6, respectively. One can see that the best accuracy for the whole tumor region as well as for the tumor core region is reached in FLAIR images. However, active tumor is most accurately detected in T1C slices.

Tab. 5.3: Accuracy of particular brain tumor structures detection in axial slices of different MR sequences.

Accuracy (in %)	Whole tumor	Tumor core	Active tumor
FLAIR	90	89	83
T2	88	89	83
T1C	83	84	81
T1	81	80	78
Multisequence	90	90	88

Tab. 5.4: Accuracy of particular brain tumor structures detection in coronal slices of different MR sequences.

Accuracy (in %)	Whole tumor	Tumor core	Active tumor
FLAIR	90	88	86
T2	85	89	86
T1C	80	83	81
T1	76	77	75
Multisequence	91	91	88

Tab. 5.5: Accuracy of particular brain tumor structures detection in axial slices of different MR sequences.

Accuracy (in %)	Whole tumor	Tumor core	Active tumor
FLAIR	94	92	88
T2	89	90	88
T1C	83	87	89
T1	80	80	78
Multisequence	93	93	92

Discussion

In this part, the supervised method for brain tumor presence detection was tested. It was evaluated for two different cases, the detection in stand-alone 2D images and slice-wise detection in 3D volumes. The former used only features extracted from the asymmetry maps, while the latter added the asymmetry-based image intensity features. Figure 5.1 shows Precision-recall curves for axial plane test set for each tumor part detection using different MR sequences

Tab. 5.6: Accuracy of particular brain tumor structures detection in coronal slices of different MR sequences.

Accuracy (in %)	Whole tumor	Tumor core	Active tumor
FLAIR	93	91	87
T2	86	90	87
T1C	80	87	88
T1	77	80	77
Multisequence	94	93	92

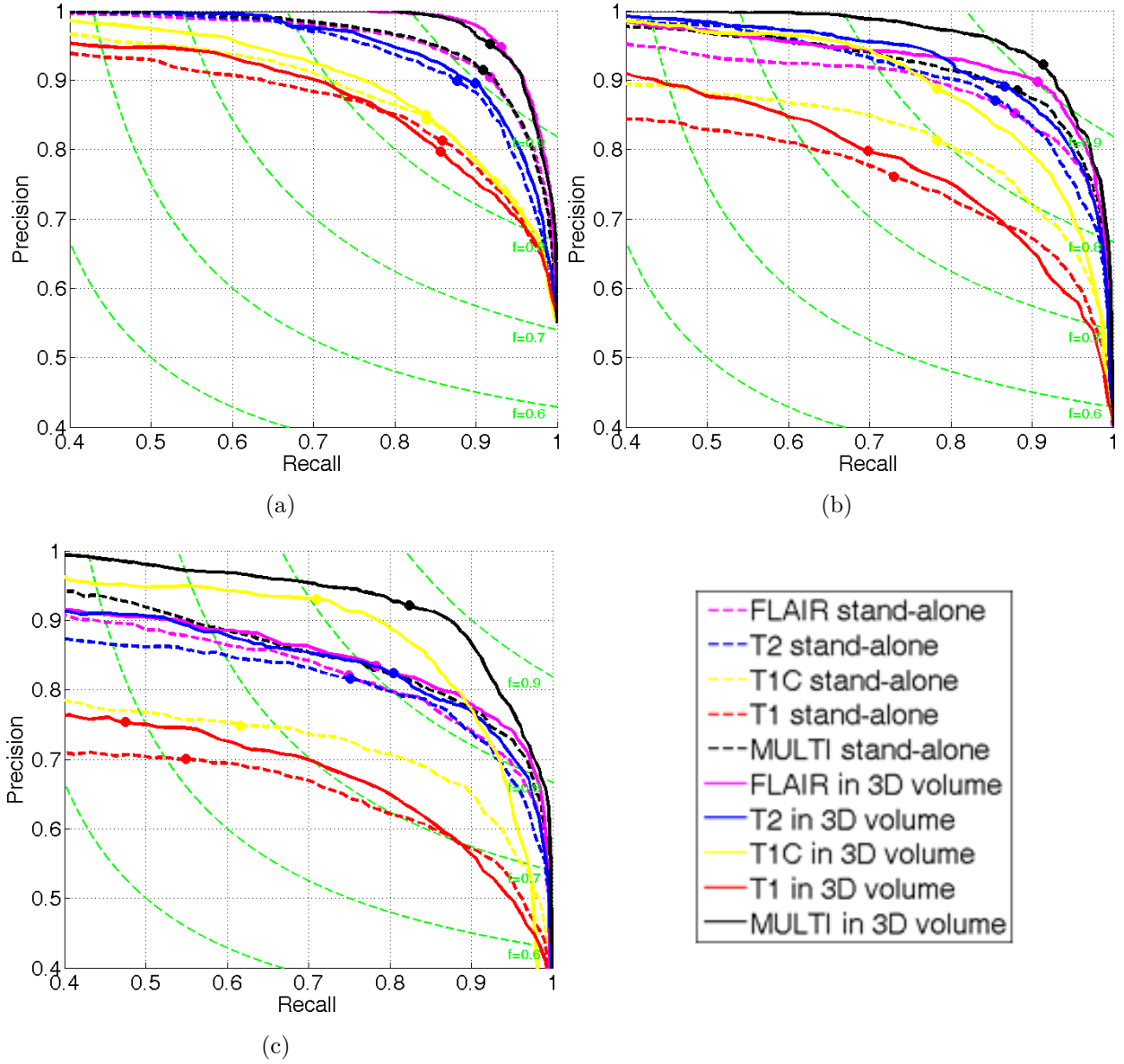
in both stand-alone slices and slices in 3D volume. Recall is equivalent to sensitivity. Green dashed curves depict isolevel lines of F-measure, which is equivalent to the Dice score. Graphs for the coronal plane are omitted since they are very similar to the graphs for the axial plane. As it can be concluded from the results, the intensity features bring important information, which in most tests improved the detection accuracy, e.g. the performance increased from 90% to 94% using axial FLAIR slices for whole tumor detection, or from 81% to 88% using coronal T1C slices for active tumor detection.

According to the results, it can be stated that in stand-alone images all parts can be automatically detected with the highest accuracy in FLAIR. In 3D volume slices, incorporating intensity-based features improves the results and active tumor is than detected with highest accuracy in T1C slices. However, using all MR sequences improves the performance in almost all detection tasks. It was shown that the algorithm reaches high accuracy in both axial and coronal planes. Since, according to the best knowledge of the author, there are no methods for the fast brain tumor presence detection task, it is not possible to compare the results with state-of-the-art algorithms.

The computing time of 0.11s per slice and sequence, where 90% of the time is consumed by symmetry analysis and the rest by feature extraction and classification, shows that this method can be used either for fast decision, whether an image contains a tumor, or in the segmentation process as a pre-processing step to determine the slices to be segment or analyzed. Many state-of-the-art methods based on deep learning architectures use slice-wise approach, and, therefore, this method can also be used in pipelines of such algorithms.

5.2 Unsupervised 2D brain tumor extraction

After the whole tumor presence is detected in 2D, it can be extracted using the novel unsupervised 2D brain tumor extraction method described in Sec. 4.2. This method is designed for FLAIR images only, therefore, other MR sequences will not be considered here.



Obr. 5.1: Precision-recall curves for (a) whole tumor, (b) tumor core and (c) active tumor presence detection in both stand-alone slices (dashed curves) and slices in 3D volume (solid curves) for the axial plane test set. Circles on each curve represent the actual achieved results. Green dashed curves depict isolevel lines of F-measure, which is equivalent to the Dice score.

Experimental setup

Since the proposed algorithm is unsupervised, i.e. no training phase is required; it was tested on the whole set of 254 FLAIR volumes. Axial and coronal slices containing a whole tumor area of at least 6cm^2 were extracted from each volume since the method cannot deal with smaller pathologies. The overall numbers of axial and coronal slices included in the test are 22213 (18445 of HG and 3768 of LG) and 28078 (23401 of HG and 4669 of LG), respectively.

Application to the test set

The results of the algorithm application to axial and coronal slices are summarized in Tab. 5.7. The table contains the overall results as well as the results achieved for high- and low-grade gliomas evaluated by the Dice score, precision and sensitivity.

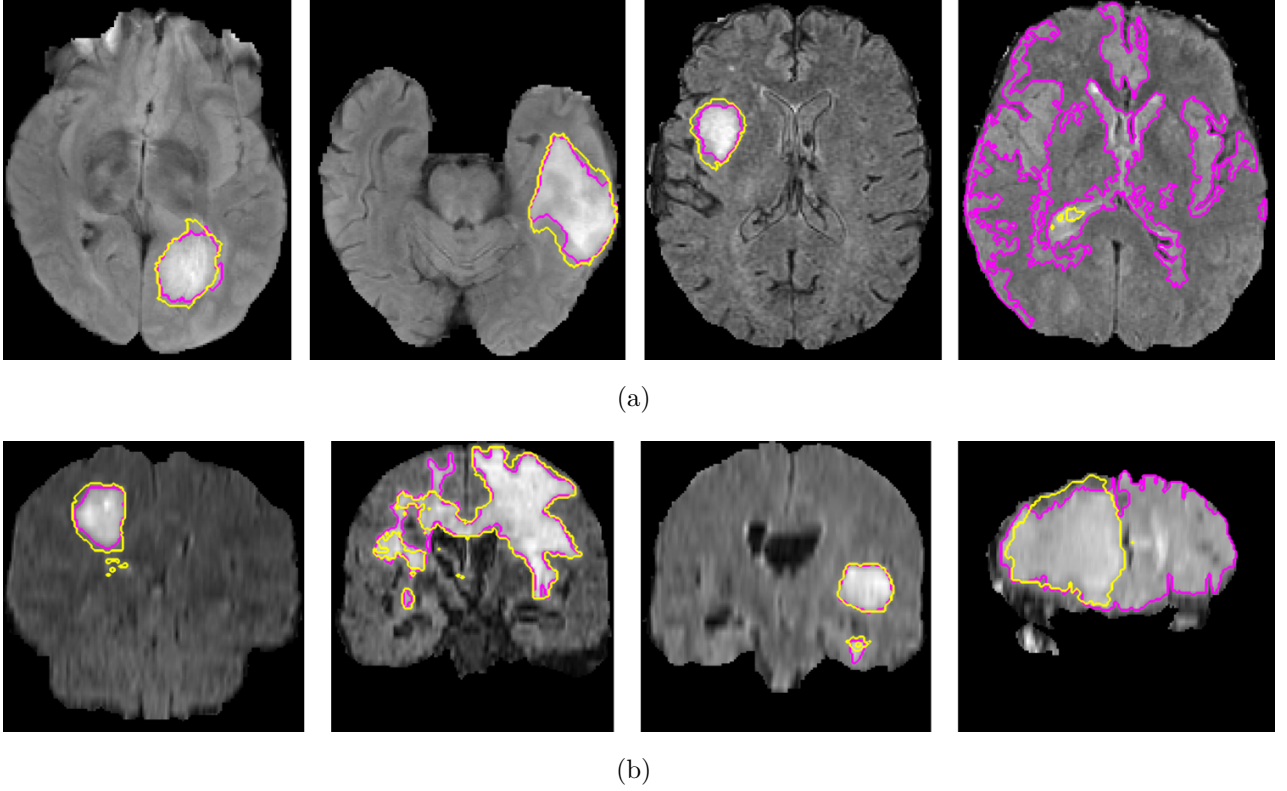
Tab. 5.7: Segmentation results reporting average and median Dice score, precision and sensitivity. Shown are results for axial and coronal slices. “std” and “mad” denote standard deviation and median absolute deviance. HG and LG stand for high- and low-grade gliomas, respectively.

	Axial		Coronal	
	HG / LG		HG / LG	
Dice Score (in %)				
mean \pm std	63 \pm 30	63 \pm 30 / 59 \pm 32	63 \pm 29	63 \pm 29 / 60 \pm 30
median \pm mad	77 \pm 27	77 \pm 27 / 76 \pm 30	76 \pm 26	78 \pm 26 / 70 \pm 28
Precision (in %)				
mean \pm std	64 \pm 37	64 \pm 37 / 57 \pm 39	63 \pm 37	65 \pm 37 / 58 \pm 38
median \pm mad	85 \pm 35	85 \pm 35 / 71 \pm 37	81 \pm 34	84 \pm 34 / 65 \pm 36
Sensitivity (in %)				
mean \pm std	87 \pm 31	87 \pm 16 / 91 \pm 12	87 \pm 15	86 \pm 15 / 91 \pm 12
median \pm mad	92 \pm 11	91 \pm 12 / 96 \pm 09	91 \pm 11	91 \pm 12 / 95 \pm 09

In the table, one can see higher sensitivity values than precision. This points to the fact that the resulting area is usually larger than the true tumor area, in other words, more false positives than false negatives are present. The sensitivity values show that in average 87% of positive pixels were found, while the precision values show that in average 64% of positive labels were truly positive. The average computing time per slice is 0.13 seconds, where 75% of the time is consumed by the symmetry analysis. Examples of the comparison of a manual annotation and an automatic extraction in both axial and coronal planes are shown in Fig. 5.2. Three successful and one unsuccessful (the most right) automatic segmentations are shown for each plane. The unsuccessful segmentation in axial plane shows the failure of the method in case of a small pathology. The algorithm was not able to correctly determine the threshold due to the small amount of tumorous pixels. The unsuccessful segmentation in coronal plane shows a failure of the method for an image where the intensities of the pathology are very similar to the intensities of healthy tissues.

Discussion

The purpose of this algorithm was to extract a tumor area (including edema) from a stand-alone FLAIR image. The results are not comparable to the state-of-the-art methods used for multisequence 3D brain tumor extraction, which are mostly based on machine learning



Obr. 5.2: Examples of the brain tumor extraction using the unsupervised algorithm in 2D (a) axial and (b) coronal FLAIR slices. A comparison of manual annotation (yellow) and automatic extraction (magenta) is depicted.

techniques using the intensity information. Such approach is possible for 3D volumes where the intensity normalization can be performed. However, this is not suitable for a stand-alone axial or coronal slice with unknown information about the tumor size and the slice coordinates. This method was designed to deal with such images and reached promising results with average and median Dice scores of 63 ± 30 and 77 ± 27 and computing time of only 0.13 seconds.

5.3 Unsupervised 3D brain tumor extraction

In this section, the method proposed for unsupervised brain tumor locating and extracting is evaluated. This method is based on a novel unsupervised algorithm combining 3D multiresolution symmetry analysis described in Sec. 4.1 and automatic thresholding.

Experimental setup

The 3D unsupervised brain tumor extraction algorithm was also tested on the whole database of 254 multisequence volumes since it does not require any training phase, and, hence, data partitioning is not necessary. This algorithm requires only T2 and FLAIR images, therefore

other MR sequences are not considered in these tests. During testing, the accuracy of the automatic tumor locating using the symmetry analysis is evaluated together with the automatic whole tumor extraction. The tumor location is determined by the maximum of the multiresolution asymmetry map. This point shows the highest probability of the tumor location and, hence, it is able to detect slices in all three planes where there is the maximum probability of the tumor presence. If this point lies within the area of a tumor, it is considered as a correct locating. Since the asymmetry map is symmetrical according to the mid-sagittal plane, i.e. two maxima exist, either of them is considered. The second test evaluates the accuracy of the whole tumor region extraction. This is evaluated by the Dice score, precision and sensitivity.

Application to the test set

Brain tumor locating. This test was performed separately for each MR sequence, i.e. T2 and FLAIR. Results for both MR sequences are summarized in Tab. 5.8. The average computing time for one sequence is 6.7 ± 0.8 seconds per volume.

Tab. 5.8: Brain tumor locating using asymmetry detection. The table expresses the percentage of correctly located brain tumors.

Accuracy (in %)	Overall	HG / LG
T2	90	90 / 90
FLAIR	95	96 / 95
T2+FLAIR	95	95 / 94

As one can see in the table, the proposed algorithm can automatically locate a tumor and show slices with a tumor within less than 7 seconds with an accuracy of 95% in FLAIR volumes and 90% in T2 volume of 1mm isotropic resolution. Combination of T2 and FLAIR volumes, where the time necessary for the asymmetry detection is twice higher, did not bring any improvement, and, hence, it can be stated that FLAIR volume is more suitable for brain tumor locating, at least in case of using the symmetry prior and the proposed approach.

An example of the tumor locating algorithm is shown in Fig. 5.3 where slices with the maximum asymmetry of all three planes are shown. The coordinates of this maximum are depicted by blue circle. The figure shows four different slices per subject. Two slices are shown in sagittal plane. The purpose is to show both slices with the maximum asymmetry, i.e. one slice from the left and one slice from the right hemisphere.

Brain tumor extraction. The performance of the brain tumor extraction algorithm based on the symmetry analysis is evaluated here by mean and median values of Dice score, precision and sensitivity. All results are summarized in Tab. 5.9. The overall performance as well as the performance for high-grade (HG) and low-grade (LG) gliomas is shown. The average

computing time is 13.8 ± 1.3 seconds per volume including the previous symmetry analysis in both volumes, which reaches about 93% of the computing time. Slightly lower performance was achieved by applying symmetry analysis only to one volume, e.g. FLAIR. However, the computing time decreased to 7.7 ± 0.9 seconds in this case.

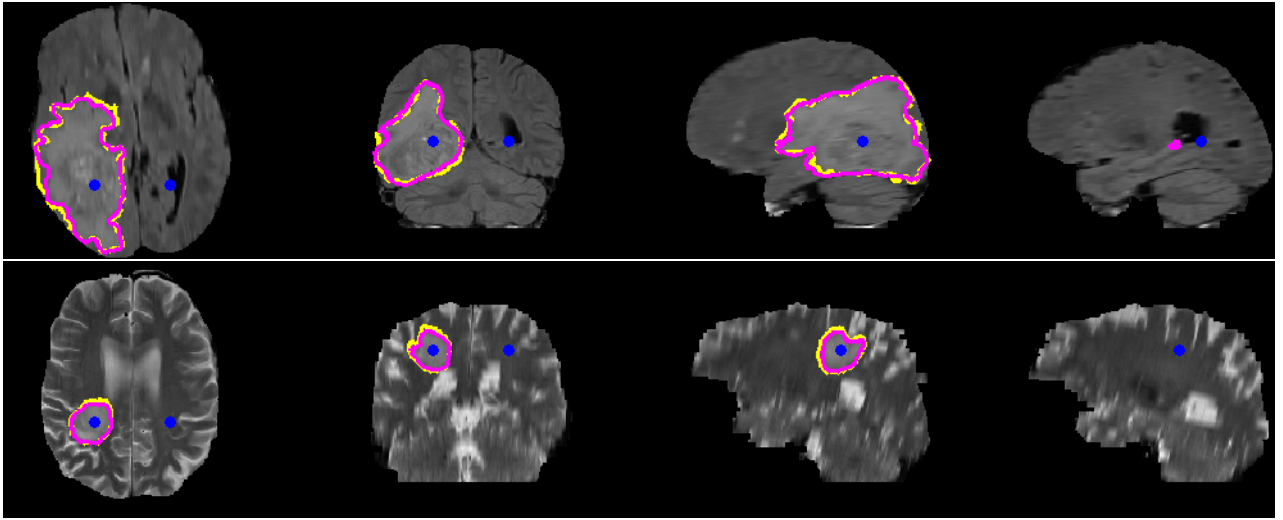
Tab. 5.9: Brain tumor extraction using asymmetry detection.

	Overall	HG / LG
Dice Score (in %)		
mean \pm std	66 ± 21	65 ± 22 / 70 ± 20
median \pm mad	74 ± 17	74 ± 17 / 75 ± 15
Precision (in %)		
mean \pm std	89 ± 22	90 ± 22 / 88 ± 23
median \pm mad	98 ± 14	99 ± 14 / 98 ± 15
Sensitivity (in %)		
mean \pm std	59 ± 21	57 ± 21 / 65 ± 22
median \pm mad	64 ± 17	62 ± 17 / 68 ± 17

Examples of the comparison between the automatic extraction and the manual annotation are given in Fig. 5.3 where manual annotations are depicted by yellow color, and the results of the automatic extraction process are shown by magenta color. The figure shows four different slices per subject. Two sagittal slices are shown. The purpose is to show both slices with the maximum asymmetry, i.e. one slice from the left and one slice from the right hemisphere.

Discussion

In this section, the unsupervised algorithm for fast brain tumor locating and extraction was tested. The unsupervised approach for the brain tumor locating and delineating was verified on FLAIR and T2 volumes of 254 subjects. The proposed method used an approach different from other state-of-the-art algorithms. Compared to them, it is not supervised and, therefore, it does not require any training phase. It cannot reach the top three state-of-the-art results reported in [21] with 79%-82% (here: 64%), but it still reached comparative results with other methods described in that paper. However, the advantage of the proposed algorithm is its speed since it is not that demanding as other methods. With 13.8 seconds, it is faster than the fastest method reported in [21], where only 3 methods out of 16 running on CPU were able to extract brain tumor in less than 8 minutes. Therefore, the proposed algorithm is suitable for fast preliminary approximate tumor extraction rather than accurate segmentation. The first part of the algorithm, i.e. brain tumor locating, is suitable for fast brain tumor locating for pre-analysis of a single-sequence volume since it may pre-analyze a single volume in less than 8 seconds.



Obr. 5.3: Examples of the unsupervised brain tumor extraction based on the multiresolution symmetry analysis. The results are demonstrated on one FLAIR (upper row) and one T2 (lower row) volume. The images show slices where the maximum asymmetry was detected with corresponding manual annotation (yellow) and automatic extraction (magenta). Blue circles point to the voxel with the highest asymmetry. Both sagittal slices with the maximum asymmetry are shown.

5.4 Brain tumor segmentation using local structure prediction

In this section, the method proposed for segmentation of particular structures of the brain tumor, i.e. whole tumor, tumor core, and active tumor, is evaluated. This method is based on an approach, whose novelty lies in the principled combination of the deep approach together with the local structure prediction in medical image segmentation task. The algorithm was described in Sec. 4.3.

Experimental setup

The algorithm is designed for a binary segmentation problem and it was applied separately to three brain tumor segmentation sub-problems: segmentation of whole tumor, tumor core and active tumor. From each training subject, 1500 random 2D multisequence image patches with corresponding label patches were extracted summing up to 244 500 training image patches. To ensure approximate balance of the database, higher probability of patch extraction was around the pathological area.

As it has been shown in [28], the computational demands of 3D CNN are still out of scope for today's computers. Therefore the volume is processed sequentially in 2D in the plane with the highest resolution, the axial plane here. Image patches from each multisequence volume

are mapped into four 2D input channels of the network. Alternatives to this basic approach have been proposed: slice-wise 3D segmentation approaches using CNN were proposed used in [28] and [29]. The former proposed using of a 2D CNN for each orthogonal plane separately. The later proposed extraction of corresponding patches for a given pixel from each orthogonal plane and mapping them as separated feature maps. In this work, both of these approaches were tested and compared to the single slice approach that was chosen here.

The parameters of the algorithm, i.e. the image patch size, the label patch dictionary size, and the label patch size were optimized separately for each sub-task on the validation set and the results of the optimization process are described in 5.4. It is followed by the description of the application to the tests set with examples of the segmentation results that are compared to manual annotations.

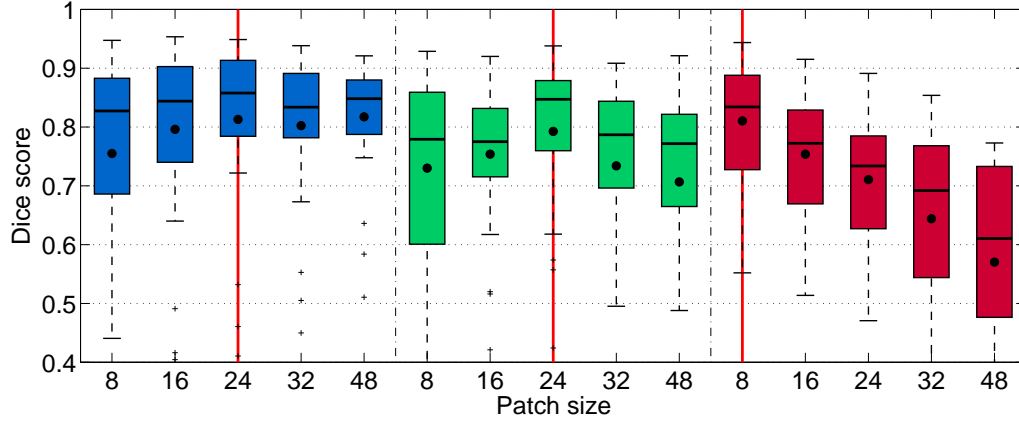
Parameter Optimization

Besides the parameters of the convolutional architecture, there are parameters of the proposed model: the image patch size d , the label patch size d' , and the size of the label patch dictionary N . These parameters were tested with a pre-optimized fixed network architecture depicted in Fig. 4.2, which consisted of two convolutional layers, both with 24 convolutional filters of kernel size 5×5 , and two mean-pooling layers in alternating order. The values selected for subsequent experiments are highlighted in graphs with a red vertical line.

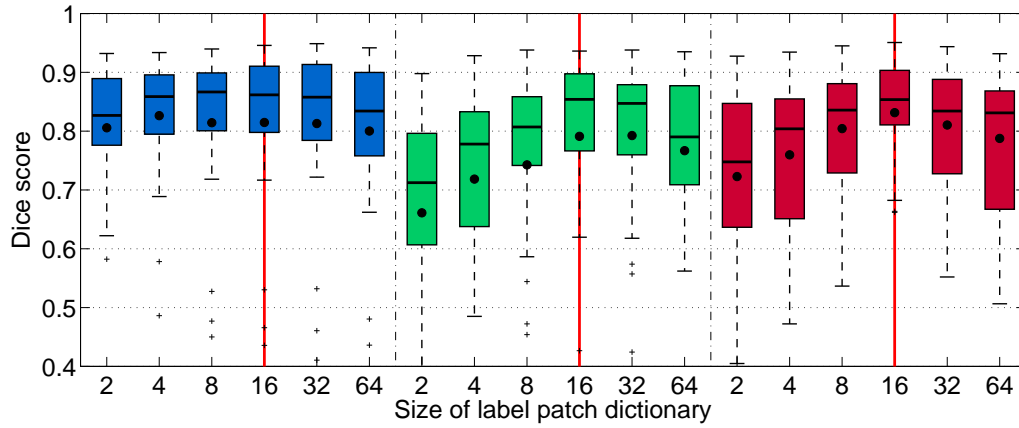
Image patch size. The image patch size d is an important parameter since the segmented structures have different sizes and therefore less or more information is necessary for the label structure prediction. Figure 5.4 shows the Dice score values for different patch sizes with their best label patch size. According to the graphs, $d = 8$ was selected for the active part segmentation and $d = 24$ for the segmentation of tumor core and whole tumor. All three tests were performed for $N = 32$, which according to the previous tests is sufficiently enough for all patch sizes. The best results were in all cases achieved for $d' \geq \frac{1}{2}d$. The values selected for subsequent experiments are indicated by a red vertical line.

Size of the label patch dictionary. The size of the label patch dictionary N influences differences between each label template \mathbf{t} as well as the differences between belonging image patches \mathbf{x} in each groups n . Results for several values of N are depicted in Fig. 5.4. Generally the best results were achieved for $N = 16$. The results were evaluated in similar manner as in the previous test, i.e. the best d' is used for each value of N . The values selected for subsequent experiments are indicated by a red vertical line.

Label patch size. The label patch size d' influences the size of structure prediction as well as the number of predictions for each voxel. Figure 5.4 shows the increasing performance with increasing d' . The values selected for subsequent experiments are indicated by a red vertical line.



Obr. 5.4: Dice score as a function of the image patch size d with its best label patch size d' and the label patch dictionary size $N = 32$ for whole tumor (blue), tumor core (green) and active tumor (red).

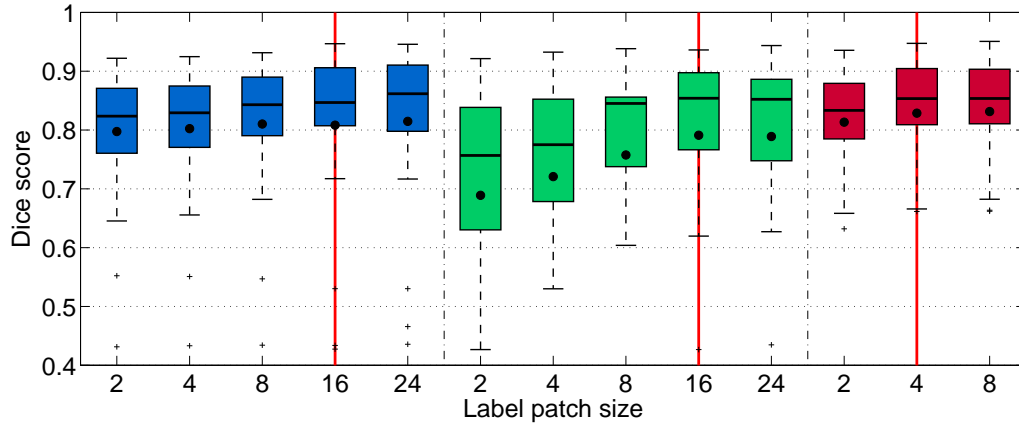


Obr. 5.5: Dice score as a function of the label patch dictionary size N using the optima of Fig. 5.4: $d = 24$ for whole tumor (blue), $d = 24$ for tumor core (green), $d = 8$ for active tumor (red).

2D versus 3D. Both triplanar and 2.5D deep learning approaches for 3D data segmentation as proposed in [28] and [29], respectively, were tested and compared to the single slice-wise segmentation approach. It was discovered that both approaches even decreased the performance of the proposed method by 2% and 5%, respectively.

Application to the test set

After the optimization of the parameters using the validation set, the algorithm was tested on a new previously unseen set of 66 random subjects from BRATS 2014. The performance for both validation and test set of all three structures is summarized in Tab. 5.10. For the test set, the achieved average Dice scores are 83% (whole tumor), 75% (tumor core), and 77% (active tumor). Tables 5.11 and 5.12 summarize precision and sensitivity of the proposed algorithm for all three segmented structures. As it can be derived from the results in these two tables,



Obr. 5.6: Dice score as a function of the label patch size d' for whole tumor (blue) with $d = 24$, tumor core (green) with $d = 24$, and active tumor (red) with $d = 8$, with label patch dictionary size $N = 16$.

the method has higher sensitivity than precision for the whole tumor region, which means that there are less false negatives than false positives, in other words the resulting area is usually larger than the true region. In average, 89% of the whole tumor area is labeled as pathological, while 81% of the resulting area is truly pathological. For tumor core and active tumor, the situation is opposite. High values of precision show that high percentage of voxels labeled as tumorous were selected as tumorous by expert too, i.e. 87% for tumor core and 85% for active tumor in average. However, the values of sensitivity are lower, especially for tumor core in case of low-grade gliomas. This means that there are less false positives than false negatives. In other words, the resulting area is smaller than the region selected manually by an expert.

Tab. 5.10: Segmentation results on validation and test data sets, reporting average and median Dice scores. Shown are the results for all three segmented structures, i.e., whole tumor, tumor core and active tumor. Scores for active tumor are calculated for high-grade cases only. “std” and “mad” denote standard deviation and median absolute deviance. HG and LG stand for high- and low-grade gliomas, respectively.

Dice Score (in %)	Whole		Core		Active
	HG / LG		HG / LG		
Validation set					
mean \pm std	81 \pm 15	80 \pm 17 / 85 \pm 06	79 \pm 13	85 \pm 08 / 65 \pm 15	81 \pm 11
median \pm mad	86 \pm 06	86 \pm 07 / 85 \pm 05	85 \pm 06	85 \pm 03 / 73 \pm 10	83 \pm 08
Test set					
mean \pm std	83 \pm 13	86 \pm 09 / 76 \pm 21	75 \pm 20	79 \pm 14 / 61 \pm 29	77 \pm 18
median \pm mad	88 \pm 04	88 \pm 03 / 87 \pm 05	83 \pm 08	82 \pm 07 / 72 \pm 14	83 \pm 09

Tab. 5.11: Segmentation results on validation and test data sets, reporting average and median precision. Shown are the results for all three segmented structures, i.e., whole tumor, tumor core and active tumor. Scores for active tumor are calculated for high-grade cases only. “std” and “mad” denote standard deviation and median absolute deviance. HG and LG stand for high- and low-grade gliomas, respectively.

Precision (in %)	Whole HG / LG		Core HG / LG		Active
Validation set					
mean \pm std	78 \pm 16	77 \pm 18 / 81 \pm 07	92 \pm 06	91 \pm 07 / 93 \pm 03	90 \pm 10
median \pm mad	84 \pm 08	83 \pm 08 / 84 \pm 08	93 \pm 03	93 \pm 03 / 92 \pm 01	92 \pm 04
Test set					
mean \pm std	81 \pm 16	83 \pm 11 / 71 \pm 25	87 \pm 13	88 \pm 13 / 86 \pm 12	85 \pm 18
median \pm mad	86 \pm 04	87 \pm 03 / 82 \pm 07	92 \pm 04	92 \pm 04 / 89 \pm 09	91 \pm 05

Tab. 5.12: Segmentation results on validation and test data sets, reporting average and median sensitivity. Shown are the results for all three segmented structures, i.e., whole tumor, tumor core and active tumor. Scores for active tumor are calculated for high-grade cases only. “std” and “mad” denote standard deviation and median absolute deviance. HG and LG stand for high- and low-grade gliomas, respectively..

Sensitivity (in %)	Whole HG / LG		Core HG / LG		Active
Validation set					
mean \pm std	87 \pm 10	84 \pm 11 / 93 \pm 04	58 \pm 26	66 \pm 22 / 35 \pm 25	71 \pm 17
median \pm mad	89 \pm 06	88 \pm 05 / 95 \pm 02	66 \pm 17	71 \pm 12 / 25 \pm 11	73 \pm 12
Test set					
mean \pm std	89 \pm 09	89 \pm 09 / 89 \pm 08	66 \pm 24	71 \pm 21 / 47 \pm 27	72 \pm 23
median \pm mad	92 \pm 03	92 \pm 02 / 90 \pm 06	71 \pm 16	78 \pm 11 / 53 \pm 17	80 \pm 12

Examples of segmentations generated by the proposed method and corresponding manual segmentations for three segmented structures on representative test cases are shown in Fig. 5.7.

Compute time vs accuracy The possibility of subsampling the volume in order to reduce the computational demands was tested here. The trade-off between accuracy and computing time per volume is analyzed in Tab. 5.13 by running several experiments with different resolutions of the CNN output before final prediction of the local structure (first column), i.e., subsampling in x and y , as well as different distances between segmented slices (second column), i.e., subsampling in z direction. All experiments were run on 4-core CPU Intel Xeon E3

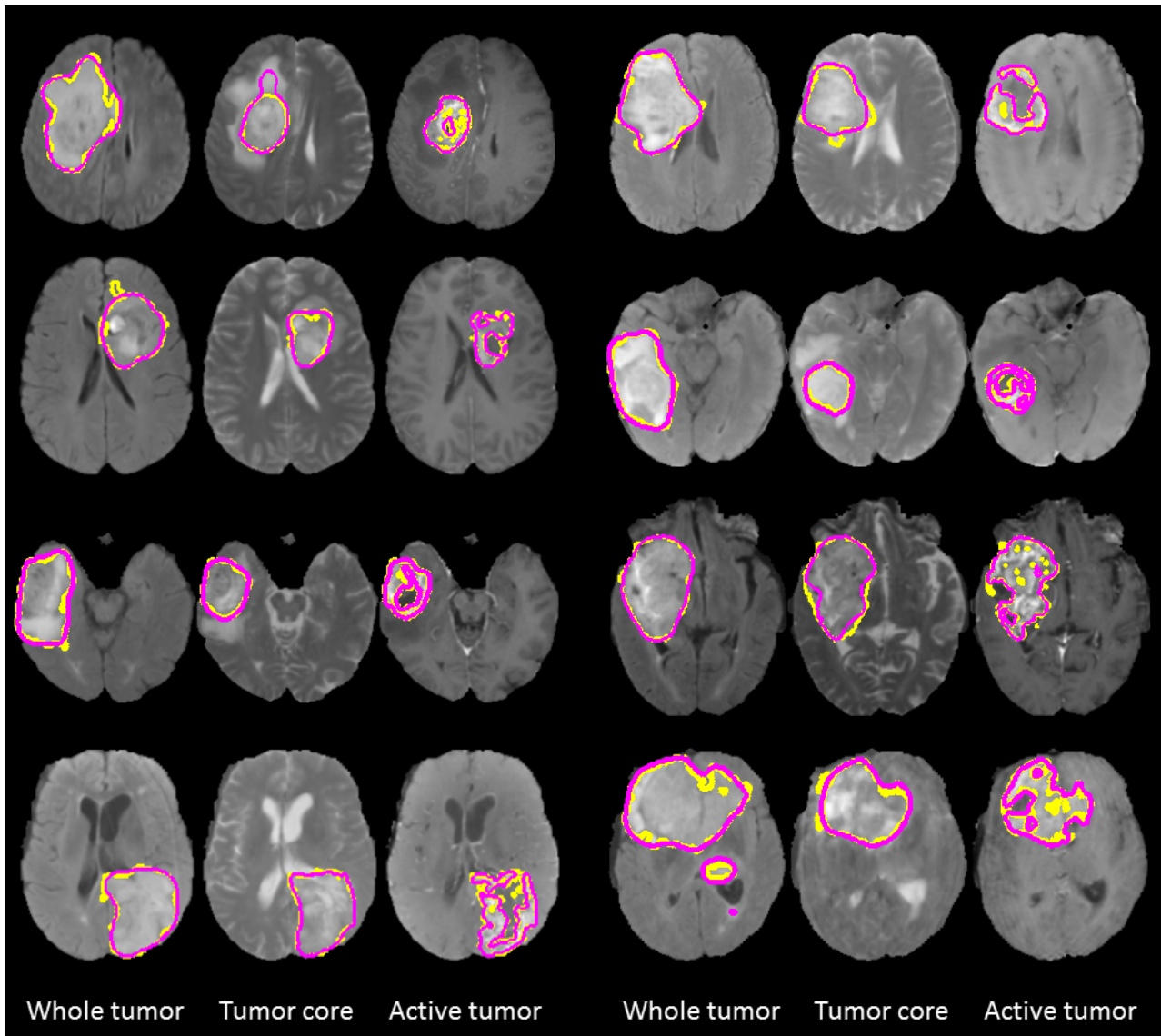
3.30GHz. As one can see in the table, the state-of-the-art results can be achieved in an order of magnitude shorter time than in case of most methods participated in BRATS challenge. Thanks to the fast implementation of the CNN classification algorithm, all three structures can be segmented in the whole volume in 13 seconds without using GPU implementation. Processing by the CNN is approximately 80% of the overall computing time, while the assignment final labels using local structure prediction requires only 17%. The rest of the time are other operations including interpolation.

Tab. 5.13: Trade-off between spatial subsampling, computing time, and segmentation accuracy. First two columns express different CNN output resolution, i.e., after subsampling in x and y , and steps between segmented slices, i.e., after subsampling in z direction.

CNN output resolution	Slice step	Computing time per volume	Dice Score (in%)		
			Whole	Core	Active
1/4	4	13s	83	75	73
1/4	2	22s	84	75	74
1/4	1	74s	84	75	75
1/2	4	24s	83	75	74
1/2	2	41s	83	75	76
1/2	1	142s	84	75	76
1/1	4	47s	83	75	75
1/1	2	80s	83	75	77
1/1	1	280s	83	75	77

Discussion

In this section, it has been shown that exploiting local structure through the use of the label patch dictionaries improves segmentation performance over the standard approach predicting voxel wise labels. It has also been shown that local structure prediction can be combined with, and improves upon, standard prediction methods, such as CNNs. When optimized for a given segmentation problem it also performs spatial regularization at the local level. On the reference benchmark set, the proposed approach achieved state-of-the-art performance even without post-processing through Markov random fields which were part of most best performing approaches in the tumor segmentation challenge. Moreover, all three structures can be extracted from the whole volume within only 13 seconds using CPU obtaining state-of-the-art results providing means, for example, to do online updates when aiming at an interactive segmentation. The resulting Dice scores are comparable to intra-rater similarity that had been reported for the three annotation tasks in the BRATS data set [21] with Dice scores 85% (whole tumor), 75% (tumor core) and 74% (active tumor) and to the best results



Obr. 5.7: Example of consensus expert annotation (yellow) and automatic segmentation (magenta) applied to the test image data set. Each row shows two cases. From left to right: segmentation of whole tumor (shown in FLAIR), tumor core (shown in T2) and active tumor (shown in T1c).

of automated segmentation algorithms with Dice scores of the top three in between 79%–82% (here: 83%) for the whole tumor segmentation task, 65%–70% (here: 75%) for the segmentation of the tumor core area, and 58%–61% (here: 77%) for the segmentation of active tumor.

6 CONCLUSION

This thesis introduced three approaches for brain tumor detection and segmentation in 2D or 3D single- and multisequence MRI. The attention was paid to high- and low-grade gliomas. All three algorithms were tested and evaluated on a large public BRATS challenge database of 254 3D multisequence subjects. with co-registered and skull-stripped FLAIR, T2, T1 and T1-contrast enhanced volumes of isotropic resolution 1mm. All data sets included manual annotations provided by experts and they were used for the evaluation of the proposed methods.

The first two approaches explored the suitability of using prior brain anatomy knowledge to detect and extract brain tumors. The first method used this information for supervised detection of a particular brain tumor structure presence in 2D single- and multisequence images in both stand-alone slices and slices in 3D volume of planes where the left-right symmetry exists, i.e. axial and coronal. When applied slice-wise to 3D volumes, more information was used and higher accuracy was achieved. For stand-alone multisequence slices, where only the information extracted from asymmetry maps was used, the detection accuracy of each structure of size $\geq 1\text{cm}^2$ was around 90%. When applied to the same slices with the use of asymmetry information together with image intensity information, which is only applicable in 3D volume, the accuracy increased to 93%. A slice was processed in only 0.11 seconds in average, which makes it suitable for the use in a pipeline of any brain tumor segmentation techniques.

The second method applied similar methodology to locate a brain tumor in a singlesequence 2D and 3D MRI followed by its extraction from a multisequence MRI in an unsupervised manner. In 2D MR, the computing time of the whole extraction process was 0.13 seconds with reached average and median Dice score of 63 ± 30 and 77 ± 27 , respectively. In 3D, the proposed method was able to locate the tumor in less than 8 seconds and extract it in about 13 seconds with reached average and median Dice score of 66 ± 21 and 74 ± 17 , respectively. Compared to other state-of-the-art algorithms, both proposed methods are not influenced by the accuracy of the intensity normalization algorithm since they are independent on the intensity range.

The third method, focused on the segmentation of whole tumor, tumor core, and active tumor, showed that exploiting local structure through the use of the label patch dictionaries improved segmentation performance over the standard approach predicting voxel-wise labels. It was shown that local structure prediction can be combined with, and improves upon, standard prediction methods, such as CNN. When the label patch size is optimized for a given segmentation task, it is capable of accumulating local evidence for a given label, and also performs a spatial regularization at the local level. The proposed approach achieved state-of-the-art performance even without sophisticated post-processing step which are part of most best performing approaches in brain tumor segmentation. Moreover, all three structures can be extracted from the whole volume within only 13 seconds using CPU obtaining state-of-the-art results providing means, for example, to do online updates when aiming at an interactive segmentation. Most medical image data consist of 3D volumes. Therefore, one of the possible future directions in the development of the local structure prediction algorithm can be an exploration of natural 3D implementation instead of slice-wise approach.

BIBLIOGRAPHY

- [1] A. Akselrod-Ballin, M. Galun, M. J. Gomori, et al. “An Integrated Segmentation and Classification Approach Applied to Multiple Sclerosis Analysis”. In: *Proc CVPR*. 2006.
- [2] A. Bhattacharyya. “On a measure of divergence between two statistical populations defined by their probability distribution”. In: *Bulletin of the Calcutta Mathematical Society* 35 (1943), pp. 99–110.
- [3] S. Chaplot, L. M. Patnaik, and N. R. Jagannathan. “Classification of magnetic resonance brain images using wavelets as input to support vector machine and neural network”. In: *Biomedical Signal Processing and Control* 1 (2006), pp. 86–92.
- [4] L.-C. Chen, G. Papandreou, and A. Yuille. “Learning a Dictionary of Shape Epitomes with Applications to Image Labeling”. In: *Proc ICCV 2013*. 2013, pp. 337–344. DOI: 10.1109/ICCV.2013.49.
- [5] J. J. Corso, E. Sharon, S. Dube, et al. “Efficient Multilevel Brain Tumor Segmentation with Integrated Bayesian Model Classification”. In: *TMI* 27(5) (2011), pp. 629–640.
- [6] A. Criminisi and J. Shotton. *Decision Forests for Computer Vision and Medical Image Analysis*. Springer, 2013.
- [7] A. Davy, M. Havaei, D. Warde-Farley, et al. “Brain Tumor Segmentation with Deep Neural Networks”. In: *Proc MICCAI-BRATS*. 2014.
- [8] P. Dollar and C. L. Zitnick. “Structured Forests for Fast Edge Detection”. In: *Proc ICCV 2013*. 2013, pp. 1841–1848.
- [9] E. Eisenhauer, P. Therasse, J. Bogaerts, et al. “New response evaluation criteria in solid tumours: Revised RECIST guideline (version 1.1)”. In: *European Journal of Cancer* 45 (2) (2009), pp. 228–247.
- [10] R. Farjam, H. A. Parmar, D. C. Noll, et al. “An approach for computer-aided detection of brain metastases in post-Gd T1-W MRI”. In: *Magn. Reson. Imaging* 30 (2012), pp. 824–836.
- [11] J. Festa, S. Pereira, J. A. Mariz, et al. “Automatic Brain Tumor Segmentation of Multi-sequence MR images using Random Decision Forests MICCAI Grand Challenge: BRATS 2013”. In: *Proc MICCAI-BRATS*. 2013.
- [12] B. J. Frey and D. Dueck. “Clustering by Passing Messages Between Data Points”. In: *Science* 315 (2007), pp. 972–976. URL: www.psi.toronto.edu/affinitypropagation.
- [13] E. Geremia, B. H. Menze, and N. Ayache. “SPATIALLY ADAPTIVE RANDOM FORESTS”. In: *Proc ISBI*. 2013.
- [14] J. E. Iglesias, E. Konukoglu, D. Zikic, et al. “Is Synthesizing MRI Contrast Useful for Inter-modality Analysis?” In: *Proc MICCAI 2013*. 2013, pp. 631–638.

- [15] A. Islam, S. M. S. Reza, and K. M. Iftekharuddin. “Multifractal Texture Estimation for Detection and Segmentation of Brain Tumors”. In: *IEEE Trans Biomed Eng.* 60 (11) (2013), pp. 3204–3215.
- [16] P. Kotschieder, S. Rota Bulò, H. Bischof, et al. “Structured class-labels in random forests for semantic image labelling”. In: *Proc ICCV 2011*. 2011, pp. 2190–2197. DOI: 10.1109/ICCV.2011.6126496.
- [17] S. K. Kyriacou, C. Davatzikos, S. J. Zinreich, et al. “Nonlinear Elastic Registration of Brain Images with Tumor Pathology Using a Biomechanical Model”. In: *TMI* 18(7) (1999), pp. 580–592.
- [18] S. Liao, Y. Gao, A. Oto, et al. “Representation Learning: A Unified Deep Learning Framework for Automatic Prostate MR Segmentation”. In: *Proc MICCAI 2013*. 2013, pp. 254–261.
- [19] Y. Liu, R. T. Collins, and W. E. Rothfus. “Robust midsagittal plane extraction from normal and pathological 3-D neuroradiology image”. In: *IEEE Transactions on Medical Imaging* 20(3) (2003), pp. 175–192.
- [20] R. Meier, S. Bauer, J. Slotboom, et al. “Appearance- and Context-sensitive Features for Brain Tumor Segmentation”. In: *Proceedings MICCAI-BRATS 2014*. 2014.
- [21] B. Menze, A. Jakab, S. Bauer, et al. “The Multimodal Brain Tumor Image Segmentation Benchmark (BRATS)”. In: *IEEE Transactions on Medical Imaging* (2014), p. 33. DOI: 10.1109/TMI.2014.2377694. URL: <https://hal.inria.fr/hal-00935640>.
- [22] B. Menze, K. van Leemput, D. Lashkari, et al. “A Generative Model for Brain Tumor Segmentation in Multi-Modal Images”. English. In: *Proc MICCAI 2010*. 2010, pp. 151–159. ISBN: 978-3-642-15744-8. DOI: 10.1007/978-3-642-15745-5_19. URL: http://dx.doi.org/10.1007/978-3-642-15745-5_19.
- [23] S. Murugavalli and V. Rajamani. “An improved implementation of brain tumor detection using segmentation based on neuro fuzzy technique”. In: *J Comput Sci* 3(110 (2007), pp. 841–846.
- [24] N. Otsu. “A Threshold Selection Method from Gray-Level Histograms”. In: *IEEE Transactions on Systems, Man and Cybernetics* 9.1 (1979), pp. 62–66. DOI: 10.1109/TSMC.1979.4310076. URL: <http://dx.doi.org/10.1109/TSMC.1979.4310076>.
- [25] P. H. O. Pinheiro and R. Collobert. “Recurrent Convolutional Neural Networks for Scene Labeling”. In: *International Conference on Machine Learning (ICML)*. 2014.
- [26] A. Pinto, S. Pereira, H. Dinis, et al. “Random decision forests for automatic brain tumor segmentation on multi-modal MRI images”. In: *Proc ENBENG 2015*. 2015.
- [27] K. M. Pohl, S. Bouix, M. Nakamura, et al. “A Hierarchical Algorithm for MR Brain Image Parcellation”. In: *TMI* 26(9) (2007), pp. 1201–1212.

- [28] A. Prasoon, K. Petersen, C. Igel, et al. “Deep feature learning for knee cartilage segmentation using a triplanar convolutional neural network”. In: *MICCAI*. 2013, pp. 246–253.
- [29] H. R. Roth, L. Lu, A. Seff, et al. “A new 2.5D representation for lymph node detection using random sets of deep convolutional neural network observations”. In: *MICCAI 2014, Part I*. 2014, pp. 520–527.
- [30] S. Ruan, S. Lebonvallet, A. Merabet, et al. “Tumor segmentation from a multispectral MRI images by using support vector machine classification”. In: *Proc ISBI*. 2007, pp. 1236–1239.
- [31] G. C. S. Ruppert, L. Teverovskiy, C. Yu, et al. “A New Symmetry-based Method for Mid-sagittal Plane Extraction in Neuroimages.” In: *International Symposium on Biomedical Imaging: From Macro to Nano*. 2011.
- [32] B. N. Saha, N. Ray, R. Greiner, et al. “Quick detection of brain tumors and edemas: A bounding box method using symmetry”. In: *Computerized Medical Imaging and Graphics* 36.2 (2012), pp. 95 –107. ISSN: 0895-6111. DOI: <http://dx.doi.org/10.1016/j.compmedimag.2011.06.001>. URL: <http://www.sciencedirect.com/science/article/pii/S0895611111000796>.
- [33] T. Tong, R. Wolz, P. Coupe, et al. “Segmentation of MR images via discriminative dictionary learning and sparse coding: Application to hippocampus labeling”. In: *NeuroImage* 76 (2013), pp. 11–23.
- [34] G. Urban, M. Bendszus, F. Hamprecht, et al. “Multi-modal brain tumor segmentation using deep convolutional neural networks”. In: *Proc MICCAI-BRATS*. 2014, pp. 31–35.
- [35] N. Zhang, S. Ruan, S. Lebonvallet, et al. “Multi-kernel SVM based classification for brain tumor segmentation of MRI multi-sequence”. In: *Proc ICIP*. 2009.
- [36] Y. Zhang, M. Brady, and S. Smith. “Segmentation of Brain MR Images Through a Hidden Markov Random Field Model and the Expectation-Maximization Algorithm”. In: *TMI* 20(1) (2001), pp. 45–57.
- [37] L. Zhu, Y. Chen, Y. Lin, et al. “Recursive Segmentation and Recognition Templates for 2D Parsing”. In: *NIPS*. 2009, pp. 1985–1992.
- [38] L. Zhu, Y. Chen, Y. Lin, et al. “Recursive segmentation and recognition templates for image parsing”. In: *IEEE PAMI* 34.2 (2012), pp. 359–371. ISSN: 0162-8828. DOI: 10.1109/TPAMI.2011.160.
- [39] D. Zikic, Y. Ioannou, M. Brown, et al. “Segmentation of Brain Tumor Tissues with Convolutional Neural Networks”. In: *Proceedings MICCAI-BRATS 2014*. 2014, pp. 36–39.

BIBLIOGRAPHY OF THE AUTHOR

- [40] R. Benes, P. Dvorak, M. Faundez-Zanuy, et al. “Multi- focus thermal image fusion”. In: *Pattern Recognition Letters* 34(5) (2013), pp. 536–544.
- [41] P. Dvorak. “Object description in images”. In: *Student EEICT Proceedings of the 17th Conference Student EEICT 2010 Volume 2*. 2011, pp. 76–78.
- [42] P. Dvorak and K. Bartusek. “Automated 3D Brain Tumor Edema Segmentation in FLAIR MRI”. In: *MAGMA - ESMRMB 2013*. 2013.
- [43] P. Dvorak and K. Bartusek. “Brain tumor locating in 3D MR volume using symmetry”. In: *Proc. SPIE 9034, Medical Imaging 2014: Image Processing, 903432*. 2014. DOI: 10.1117/12.2042845.
- [44] P. Dvorak and K. Bartusek. “Fully Automatic 3D Glioma Extraction in Multi- contrast MRI”. In: *International Conference on Image Analysis and Recognition*. 2014, pp. 239–246.
- [45] P. Dvorak and K. Bartusek. “Multi-parametric segmentation of MR images of the Brain”. In: *9th International Conference on Measurement*. 2013, pp. 125–128.
- [46] P. Dvorak, K. Bartusek, and E. Gescheidtova. “Automatic Extraction of Pathological Area in 2D MR Brain Scan”. In: *PIERS 2014*. 2014, pp. 1885–1889.
- [47] P. Dvorak, K. Bartusek, and E. Gescheidtova. “Automatic Segmentation of Multi- Contrast MRI Using Statistical Region Merging”. In: *PIERS 2014*. 2014, pp. 1865–1869.
- [48] P. Dvorak, K. Bartusek, and W. G. Kropatsch. “Automated Segmentation of Brain Tumor Edema in FLAIR MRI Using Symmetry and Thresholding”. In: *Progress in Electromagnetics Research Symposium*. 2013, pp. 936–939.
- [49] P. Dvorak, K. Bartusek, and W. G. Kropatsch. “Pathological Area Detection in MR Images of Brain”. In: *Elektrorevue* 4(1) (2013), pp. 17–21.
- [50] P. Dvorak, K. Bartusek, W. G. Kropatsch, et al. “Automated Multi- Contrast Brain Pathological Area Extraction from MR Images”. In: *Journal of Applied Research and Technology* 13(1) (2015), pp. 58–69.
- [51] P. Dvorak, K. Bartusek, and Z. Smekal. “Unsupervised Pathological Area Extraction Using 3D T2 and FLAIR MR Images”. In: *Measurement Science Review* 14(6) (2014), pp. 357–364.
- [52] P. Dvorak, V. Juras, and W. Vogl. “Interactive Hip Joint Cartilage Segmentation”. In: *PIERS 2014*. 2014, p. 1563.
- [53] P. Dvorak, V. Juras, W. Vogl, et al. “Interactive segmentation of Hip Joint Cartilage”. In: *PIERS 2014*. 2014, pp. 2369–2372.

- [54] P. Dvorak, W. Kropatsch, and K. Bartusek. “Automatic detection of brain tumors in MR images”. In: *Telecommunications and Signal Processing (TSP), 2013 36th International Conference on*. 2013, pp. 577–580. DOI: 10.1109/TSP.2013.6614000.
- [55] P. Dvorak and W. G. Kropatsch. “Detection of Brain Tumors Based on Automatic Symmetry Analysis”. In: *Proceedings of the 18th Computer Vision Winter Workshop*. 2013, pp. 24–31.
- [56] P. Dvorak, W. G. Kropatsch, and K. Bartusek. “Automatic Brain Tumor Detection in T2-weighted Magnetic Resonance Images”. In: *Measurement Science Review* 13(5) (2013), pp. 223–230.
- [57] P. Dvorak and B. H. Menze. “Structured Prediction with Convolutional Neural Networks for Multimodal Brain Tumor Segmentation”. In: *Proceedings MICCAI-MCV 2015*. 2015 (accepted).
- [58] P. Dvorak, J. Mikulka, and K. Bartusek. “Tissue Segmentation of Brain MRI”. In: *37th International Conference on Telecommunications and Signal Processing 2014*. 2014, pp. 482–485.
- [59] P. Dvorak and M. Zukal. “Description of Objects in Images Using MPEG- 7 Descriptors”. In: *Eletrorrevue* 3(1) (2012), pp. 26–31.
- [60] J. Mikulka and P. Dvorak. “Fast Calculation of T2 Relaxation Time in Magnetic Resonance Imaging”. In: *PIERS 2014*. 2014, pp. 2331–2335.
- [61] J. Mikulka, P. Dvorak, and K. Bartusek. “Support Vector Machines in MR Images Segmentation”. In: *9th International Conference on Measurement*. 2013, pp. 157–160.
- [62] M. Zukal, P. Dvorak, and P. Cika. “Implementation of MPEG-7 Descriptors”. In: *13th International Conference on Research in Telecommunication Technologies 2011*. 2011, pp. 127–130.

Curriculum Vitae

Pavel Dvořák

Personal information:

Address: Přísnovice, Czech Republic
E-mail: pavel.dvorak@hotmail.com
GSM: +420 777 057 705

School and education:

09/2011-present Brno University of Technology, Faculty of Electrical Engineering and Communication
Ph.D.
09/2009-06/2011 Brno University of Technology, Faculty of Electrical Engineering and Communication
MSc.
07/2004-06/2007 Brno University of Technology, Faculty of Electrical Engineering and Communication
BSc.

Work experience:

01/2013-present Junior Researcher, Brno University of Technology
02/2013-present Junior Researcher, Czech Academy of Sciences

Research stays:

07/2015-08/2015 Escola Universit ria Polit cnica de Matar , Spain
09/2014-03/2015 Chair for Computer Aided Medical Procedures & Augmented Reality, Technical University Munich, Germany
03/2014-08/2014 Private University of Health Sciences, Medical Informatics and Technology, Austria
12/2013-01/2014 Center of Medical Physics and Biomedical Engineering, Medical University of Vienna, Austria
09/2013-11/2013 MR Centre of Excellence, Medical University of Vienna, Austria
09/2012-12/2012 Pattern Recognition and Image Processing Group, Vienna University of Technology, Austria
06/2012-07/2012 Escola Universit ria Polit cnica de Matar , Spain
11/2011-12/2011 Escola Universit ria Polit cnica de Matar , Spain

Project participation:

04/2014-present	LD14091, Primary and secondary biometrical and non-biometrical features in the process of de-identification of audio-visual content in multimedia data
01/2014-present	FEKT-S-14-2335: Cognitive multimedia analysis of audio and image signals
02/2013–12/2014	GAP102/12/1104, Study of metabolism and localization of primary brain tumors using MR imaging techniques
02/2013–12/2013	GAP102/12/1104, Study of metabolism and localization of primary brain tumors using MR imaging techniques
01/2013-12/2013	ED2.1.00/03.0072, Center of Sensor, Information and Communication Systems
01/2012-12/2014	FEKT-S-11-17: Research of Sophisticated Methods for Digital Audio and Image Signal Processing

Awards:

2011	Dean's award for the master's thesis Object Description in Images
2011	Master Degree with Distinction

Publications:

- Papers published in journals with impact factor: 4
- Papers published in other journals: 2
- Papers published in international conference proceedings: 13
- Papers published in domestic conference proceedings: 1
- Abstracts published in international conference proceedings: 2
- Papers indexed in WoS: 5
- Papers indexed in Scopus: 11
- H-index according to WoS: 1
- H-index according to Scopus: 3

ABSTRACT

This work deals with the brain tumor detection and segmentation in multisequence MR images with particular focus on high- and low-grade gliomas. Three methods are proposed for this purpose. The first method deals with the presence detection of brain tumor structures in axial and coronal slices. This method is based on multi-resolution symmetry analysis and it was tested for T1, T2, T1C and FLAIR images. The second method deals with extraction of the whole brain tumor region, including tumor core and edema, in FLAIR and T2 images and is suitable to extract the whole brain tumor region from both 2D and 3D. It also uses the symmetry analysis approach which is followed by automatic determination of the intensity threshold from the most asymmetric parts.

The third method is based on local structure prediction and it is able to segment the whole tumor region as well as tumor core and active tumor. This method takes the advantage of a fact that most medical images feature a high similarity in intensities of nearby pixels and a strong correlation of intensity profiles across different image modalities. One way of dealing with – and even exploiting – this correlation is the use of local image patches. In the same way, there is a high correlation between nearby labels in image annotation, a feature that has been used in the “local structure prediction” of local label patches. Convolutional neural network is chosen as a learning algorithm, as it is known to be suited for dealing with correlation between features.

All three methods were evaluated on a public data set of 254 multisequence MR volumes being able to reach comparable results to state-of-the-art methods in much shorter computing time (order of seconds running on CPU) providing means, for example, to do online updates when aiming at an interactive segmentation.